The Predictive Skills of Elastic Coulomb Rate-and-state Aftershock Forecasts During the 2019 Ridgecrest, California, Earthquake Sequence

S. Mancini [1,2], M. Segou [2], M. J. Werner [1], and T. Parsons [3]

[1] School of Earth Sciences, University of Bristol, BS8 1RL Bristol, UK
[2] British Geological Survey, Lyell Centre, EH10 4AP, Edinburgh, UK
[3] United States Geological Survey, Moffett Field, California, USA

Corresponding author: Simone Mancini (simone.mancini@bristol.ac.uk)

Abstract

Operational earthquake forecasting protocols commonly use statistical models for their recognized ease of implementation and robustness in describing the short-term spatiotemporal patterns of triggered seismicity. However, recent advances on physics-based aftershock forecasting reveal comparable performance to the standard statistical counterparts with significantly improved predictive skills when fault and stress field heterogeneities are considered. Here, we perform a pseudo-prospective forecasting experiment during the first month of the 2019 Ridgecrest (California) earthquake sequence. We develop seven Coulomb rate-and-state models that couple static stress change estimates with continuum mechanics expressed by the rate-and-state friction laws. Our model parametrization supports a gradually increasing complexity; we start from a preliminary model implementation with simplified slip distributions and spatially homogeneous receiver faults to reach an enhanced one featuring optimized fault constitutive parameters, finite-fault slip models, secondary triggering effects, and spatially heterogenous planes informed by pre-existing ruptures. The data-rich environment of Southern California allows us to test whether incorporating data collected in near real-time during an unfolding earthquake sequence boosts our predictive power. We assess the absolute and relative performance of the forecasts by means of statistical tests used within the Collaboratory for the Study of Earthquake Predictability (CSEP) and compare their skills against a standard benchmark ETAS model for the short (24 hours after the two Ridgecrest mainshocks) and intermediate-term (one month). Stress-based forecasts expect heightened rates along the whole near-fault region and increased expected seismicity rates in Central Garlock Fault. Our comparative model evaluation supports that faulting heterogeneities coupled with secondary triggering effects are the most critical success components behind physics-based forecasts, but also underlines the importance of model updates incorporating

near real-time available aftershock data reaching better performance than standard ETAS. We explore the physical basis behind our results by investigating the localized shut down of pre-existing normal faults in the Ridgecrest near-source area.

Introduction

On 4 July 2019, a Mw 4.0 earthquake occurred in the Searles Valley (Southern California) and was followed within ~30 minutes by a Mw 6.4 event. Just 34 hours later, on 6 July, a Mw 7.1 earthquake struck near the town of Ridgecrest approximately 10 km NE of the Mw 6.4 epicenter. The 2019 Ridgecrest earthquakes belong to the Eastern California Shear Zone (ECSZ), where large magnitude seismicity had not been observed since the 1999 Mw 7.1 Hector Mine event. The two earthquakes nucleated on a system of orthogonal strike slip faults (Figure 1): northeast-trending left-lateral for the Mw 6.4 event and northwest-trending right-lateral for the Mw 7.1 mainshock. The activated area is located in the vicinity of the Airport Lake and Little Lake fault zones, characterized by distributed faulting with mainly right-lateral strike slip and normal kinematics (*Bryant*, 2017). The resulting cascade of aftershocks involved several subparallel faults that cumulatively exceeded 75 km in length (*Barnhart et al.*, 2019; *Ross et al.*, 2019; *Chen et al.*, 2020).

The Ridgecrest area has previously experienced moderate magnitude earthquakes, including the 1982 Mw 5.2 Indian Wells Valley event and the 1995-1996 sequence with three M5+ shocks, the first two of which occurred five weeks apart. The 1995 earthquakes exhibited similar complexity to the 2019 events, with triggered seismicity on normal and strike-slip northwest and northeast trending faults (*Hauksson et al.*, 1995).

The tectonic setting of the epicentral region, bounded by the Garlock system to the south and extending towards the Owens Valley fault to the north (Figure 1), where moderate to large

magnitude earthquakes occurred in the last ~150 years (including the 1872 M≈7.5 Owens Valley earthquake), immediately raised severe concerns on whether the occurrence of the July 2019 events could promote the nucleation of large events on nearby faults, as previously observed in the ECSZ (*e.g.* the 1992 Landers sequence).

Among the physics-based approaches employed to model the expected rate of triggered seismicity due to fault-to-fault interactions, Coulomb rate-and-state (CRS) forecasts combine the calculation of the static stress changes cast by an earthquake in the surrounding crustal volume (*Harris & Simpson*, 1992) with laboratory-derived rate-and-state constitutive laws (e.g. *Dieterich*, 1994) that describe the fault's frictional response to the imparted stresses. Recent work on the improvement of such physics-based forecasts within the 2016-2017 Central Apennines (Italy) earthquake sequence showed that the predictive skills of CRS models increase when crustal and stress field heterogeneity resulting from past focal mechanisms and secondary earthquake triggering is considered (*Mancini et al.*, 2019). The 2019 Ridgecrest sequence presents a unique opportunity to further test the performance of CRS forecasts and advance our understanding of model features that improve short-term aftershock forecasts in high-hazard settings with complex rupture patterns and diverse population of triggered seismicity. In the era of machine learning catalogs that promise future improvements in real-time earthquake detection (e.g. *Ross et al.*, 2018; *Mousavi et al.*, 2019), we investigate whether physics-based forecasts can benefit from the inclusion of sequence-specific data. Hence, we extend previous work by testing if the predictive power of Coulomb rate-and-state forecasts increases when we update fault models using evolving aftershock data.

Here we perform a pseudo-prospective experiment, that is, the issued models follow approximately the evolution of near real-time data availability and quality. Focusing on their

overall predictive power and their spatial consistency, we present the absolute and relative performance of the forecasts for the first month following the Mw 6.4 Searles Valley earthquake, making use of the well-established evaluation metrics introduced by the Collaboratory for the Study of Earthquake Predictability (CSEP – *Jordan*, 2006; *Michael & Werner*, 2018). To benchmark the CRS models, we produce a basic realization of a statistical Epidemic Type Aftershock Sequence model (ETAS – *Ogata*, 1998), which currently represents the most robust and widely used modelling tool for Operational Earthquake Forecasting (OEF; *Jordan et al.*, 2011, 2014).

Data

We develop the earthquake forecasts on a testing region (Figure 1) centered on the Mw 7.1 mainshock epicenter and extending equally E-W and N-S for ~160 km (three time its rupture length). We discretize the models using a three-dimensional grid with 2 km spacing between 0-28 km of depth. Our target seismicity is the real time catalog of 1812 M2.5+ aftershocks reported in the USGS Advanced National Seismic System Comprehensive Catalog (ComCat; *Guy et al.*, 2015) for the month following the Mw 6.4 Searles Valley event (testing phase, July 4th – August 4th 2019). As a pre-Ridgecrest learning phase (to calibrate models) we consider the seismicity between January 1st 1981 – July 3rd 2019 by merging the 1981-2018 relocated catalog by *Hauksson et al.* (2012) with the ComCat events covering the last six months before the Ridgecrest sequence (43986 events in total with M2.5+). While we adopt the catalog of focal mechanisms by *Yang et al.* (2012) as evidence of the past local rupture styles in the testing region, we use the focal mechanism solutions from the Southern California Earthquake Data Center (SCEDC) as a real-time database. To constrain the faulting style on the main regional faults, we use the rupture parameters reported

in the third version of the Uniform California Earthquake Rupture Forecast (UCERF3; *Dawson*, 2013), and we assign the larger scale off-fault rupture kinematics using the smoothed stress inversion from focal mechanisms and topography by *Luttrell and Smith-Konter* (2017), which is one of the available SCEC Community Stress Models (CSM).

To calculate the static coseismic stress changes after the Mw 7.1 mainshock we use the preliminary finite-fault slip model version issued on the USGS event information webpage, which provides near real-time automated source characterization. For the Mw 6.4 event and for all those earthquakes with a focal mechanism solution, we create a synthetic uniform slip distribution within a planar surface implementing the empirical equations of *Wells and Coppersmith* (1994) to calculate the approximate fault dimensions and the relation by *Hanks and Kanamori* (1979) to estimate the amount of slip given the event magnitude.

Methods

Coulomb rate-and-state modelling

Among the sources of stress perturbations, our CRS models include static stress changes and do not account for the effect of other known physical mechanisms such as dynamic stress changes, afterslip or poro-elastic effects that may as well contribute to the triggering process at different spatiotemporal scales.

For the calculation of the Coulomb stress changes (ΔCFF) we assume an elastic halfspace medium (*Okada*, 1992) with shear modulus of 30 GPa and Poisson's ratio ν=0.25 as representative values for the upper crust. We adopt the definition of *Rice* (1992):

$$\Delta CFF = \Delta\tau + \mu'(\Delta\sigma), \quad (1)$$

where $\Delta\tau$ is the change in shear stress resolved on a given fault geometry (commonly known as "receiver fault") and set positive in direction of fault slip, $\Delta\sigma$ is the change in normal stress (positive when the fault is unclamped), $\mu' = \mu(1 - B)$ is the effective coefficient of friction, with B the Skempton's coefficient describing pore pressure changes in response to a change in applied stress. Here, all developed and tested models feature μ' = 0.4 (*Toda et al.*, 2005), but we address the uncertainty on μ' values in the supplemental material.

As the Coulomb stress hypothesis alone does not account for the time dependency of seismicity, to estimate the expected rates of earthquake production we choose to couple the coseismic static stress change calculations with rate-and-state friction constitutive laws, as they have so far represented a widely used and successful physical framework. Although more recent reviews of the rate-and-state model have been proposed (e.g. *Heimisson and Segall*, 2018), our approach implements the standard formulation by *Dieterich* (1994). According to the latter, the spatiotemporal seismicity rate evolves as:

$$R(t, x, y) = \frac{r_0(x, y)}{\gamma(t)\dot{\tau}}, \tag{2}$$

where r_0 represents the background seismicity rate, $\dot{\tau}$ is the secular shear stressing rate (that is, it is assumed to remain unvaried) and γ is a variable that under stable conditions corresponds to:

$$\gamma_0 = \frac{1}{\dot{\tau}}. \tag{3}$$

When a stress perturbation is applied to the population of receiver faults, the state variable instantaneously assumes a new value:

$$\gamma_n = \gamma_{n-1} \exp\left(\frac{-\Delta S}{A\sigma}\right), \tag{4}$$

where $A\sigma$ is the effective normal stress acting on the receiver fault, ΔS is the stress imparted by the earthquake, and γ_n and γ_{n-1} represent the values of the γ variable before and after the stress

change, respectively. While in the *Dieterich* (1994) formulation the applied stress change is the shear stress change, CRS modelling usually assumes it to be a "modified" Coulomb stress change (*Dieterich et al.*, 2000) that also includes the contribution of the effective normal stress changes. This is achieved by considering $S = \tau - (\mu - \alpha)(1 - B)\sigma$, with α a positive non-dimensional constitutive parameter controlling perturbations in normal stress (*Linker & Dieterich*, 1992). To approximate S in equation (4) to the Coulomb stress change as traditionally defined in equation (1), we assume that $\mu' = (\mu - \alpha)(1 - B)$.

Dieterich (1994) and *Dieterich et al.* (2000) show that the state variable evolves as:

$$d\gamma = \frac{1}{A\sigma}[dt - \gamma dS]. \tag{5}$$

Following equation (4), a positive stress change causes a drop of the γ value and consequently a higher earthquake rate according to equation (2). However, the seismicity rate eventually recovers as the state variable evolves in time according to *Dieterich* (1994):

$$\gamma_{n+1} = \left(\gamma_n - \frac{1}{\dot{\tau}}\right) \exp\left(\frac{-\Delta t \dot{\tau}}{A\sigma}\right) + \frac{1}{\dot{\tau}}\ , \tag{6}$$

where Δt is the time step.

In the *Dieterich's* (1994) rate-and-state framework, the ratio between the normal stress $A\sigma$ and the secular shear stressing rate $\dot{\tau}$ is the aftershock recovery time (t_a) required for the seismicity rate R to return to the background value r_0 through an Omori-like decay:

$$t_a = \frac{A\sigma}{\dot{\tau}}. \tag{7}$$

Here, we present seven models for Coulomb rate-and-state forecasts, that we implement using the parallel code by *Cattania and Khalid* (2016). We issue successive realizations by gradually introducing one or more levels of complexity in terms of model parameterizations and fault and source heterogeneities (*i.e.* each model preserves all the characteristics of the previous

one, changing/introducing only those specified in its denomination). Using a more technical term, we conduct a 'pseudo-prospective' experiment where we test the effectiveness of different Coulomb rate-and-state forecasts that evolve from preliminary to progressively more elaborated parameterizations according to near-real time data availability. We update all the forecasts at time windows (dt) of 24 hours or when a M6+ event occurs (whichever comes sooner), for a total forecast horizon of 1 month. It is worth pointing out that we do not parameterize models using the same data sample they are meant to forecast and that we estimate the next day seismicity rates out of sample. In other words, the models neither know nor use any next-day seismicity information to tune their components. Here, all CRS models are developed simultaneously, so that our modelling choices for the more enhanced realizations are not biased by the performance of the earlier versions. CRS model characteristics are summarized in Table 1.

The first CRS model, CRS1-*basic*, is the most preliminary version featuring: (1) stress changes imparted only by the Mw 6.4 and Mw 7.1 events, for which we implement a uniform slip distribution tapered at the edges of the fault from the real-time kinematic parameters provided by the SCEDC; (2) simplified receiver plane geometry, spatially uniform (SUP) and parallel to the Mw 7.1 fault which is consistent with the main regional regime; (3) spatially variable background rate (r_0) after stochastic declustering (*Zhuang et al.*, 2002) of the learning phase seismicity catalog (1981-2019), smoothed in space using the adaptive kernel method of *Helmstetter et al.* (2007); (4) rate-and-state parameters averaged from the previous work of *Toda et al.* (2005), who investigated the fingerprint of stress transfer by tuning parameters to Southern California seismicity during a subset (1986-2003) of our learning phase window.

In CRS2-*optimized* we optimize the constitutive parameters during the learning phase catalog by maximizing the log-likelihood function of *Zhuang et al.* (2012). The grid search spans

[0.01-0.1] MPa for Aσ and [1-300] years for t_a and includes the stress changes due to the past M4+ events within the testing region during the 1981-2019 window. To account for early catalog incompleteness, the fitting routine ignores the first 20 minutes after each stress-perturbing earthquake, corresponding to the best fitting Omori c-value obtained for our ETAS model (see Table S1).

CRS3-*FFM/SSI* introduces two features, namely the implementation of the near real-time USGS finite-fault slip model (FFM) for the Mw 7.1 mainshock (while no slip inversion was available for the Mw 6.4 event) and a first order structural heterogeneity of the receiver faults (spatially variable planes – SVP) in the form of: (1) in off-fault regions, planes informed from the smoothed stress inversion (SSI) from focal mechanisms and topography by *Luttrell and Smith-Konter* (2017), and (2) at the fault-specific scale, mapped UCERF3 fault geometries with kinematic parameters assigned following the USGS Fault Database in polygons extending ±2.5 km around the rupture traces, with the exception of the Garlock Fault System where we consider a 5 km buffer. The inclusion of UCERF3 rupture parameters allows accounting for well-known extensional normal faults, such as the Kern Canyon and Tank Canyon, oblique-normal faults such as the Independence Fault, right-lateral faults such as the Owens Valley, and left-lateral faults related with the Garlock Fault System.

To resolve the evolving coseismic stress field in greater detail, CRS4-*secondary* incorporates secondary triggering effects due to the stress changes following each M2.5+ aftershock. Except for the Mw 7.1 mainshock, which has an associated finite-fault model, we implement uniform slip distributions from the SCEDC real-time catalog of focal mechanisms with random selection of nodal planes, and we adopt a magnitude-dependent isotropic stress field for all those events without any available rupture characterization (*Chen et al.*, 2013):

$$\Delta \mathrm{CFF} = \frac{\mathrm{M}_0}{6\pi \mathrm{r}^3}, \quad (8)$$

In CRS5-*past_FMs* we introduce the representation of the second order structural complexities by resolving the stress changes on the diverse small-scale receiver fault populations of the area informed from pre-sequence focal mechanisms (1981-2019). We assign kinematic rupture parameters to each grid cell hosting at least one focal mechanism following a 3D nearest neighbor association and using the focal plane provided by the *Yang et al.* (2012) catalog.

The preliminary slip model version available on the USGS event webpage reaches a depth of 28 km and is explicitly affected by (1) a deep (~23 km) slip patch artifact on the north-western fault edge, and (2) an excessive fault length of about 160 km, extending well beyond the Garlock Fault to the SE and the Independence Fault to the NW. To overcome the limitations imposed by this near real-time data product, in model CRS6-*eFFM* we edit the USGS model (eFFM) by setting the rupture length according to the ShakeMap fault trace and extrapolating a vertical extension of 17 km using the empirical relations of *Wells and Coppersmith* (1994). We chose to include both results to highlight the importance of real-time data quality control for automated operational forecasting.

CRS7-*new_FMs* is the most complex among our physics-based forecasts. In this model, we make use of those fault planes that are gradually revealed by aftershocks to resolve the evolving near-source coseismic stress changes. Here, the available real-time SCEDC focal mechanism of a given aftershock replaces the receiver plane earlier assigned to the relative grid point following a criterion of proximity to the center of its cell. We update the 3D receivers' matrix by performing such nearest neighbor re-assignment of aftershock nodal planes every time the forecast is updated.

We also present three additional sensitivity tests. First, to evaluate the effect of real-time data selection, we produce an alternative model version, CRS7-*usgs*, where we use the USGS

catalog of focal mechanisms for both the computation of the synthetic slip models and the receiver faults update instead of the SCEDC one. This choice is motivated by the discrepancies between the kinematic parameters of the mainshocks reported in real-time by the SCEDC and the USGS, with special concern about the Mw 6.4 earthquake (∼20° difference in strike). Moreover, we assess how the overall spatial performance of our more complex CRS realization changes when the r_0 value in equation (2) is defined by means of an undeclustered seismicity catalog (known as 'reference rate'). We perform this test in the wake of rederivations of the Dieterich's model suggesting that initial conditions for populations of seismic sources should also account for the long-term seismicity interactions (*Heimisson*, 2019). Finally, we test the effect of implementing a different coefficient of effective friction in model CRS7-*new_FMs*.

The ETAS model

The Epidemic Type Aftershock Sequence (ETAS) model was first introduced by *Ogata* (1988) to describe the occurrence times and magnitudes of triggered seismicity and it was successively extended into the spatial domain by *Ogata* (1998). Given their relatively simple formulations and considerable performance, different versions of ETAS models are currently employed by government agencies in several countries, including California (*Field et al.*, 2017), Italy (*Marzocchi et al.*, 2014), New Zealand (*Gerstenberger and Rhoades*, 2010), and Japan (*Omi et al.*, 2019). Past and present initiatives, such as the Working Group of California Earthquake Probabilities (WGCEP), Uniform California Earthquake Rupture Forecast (UCERF) and the Collaboratory for the Study of Earthquake Probability (CSEP) tested the predictive skills of ETAS models under different implementations for short- and long-term time horizons supporting that moderate events in California occur near locations of small earthquakes (e.g. *Werner et al.*, 2011)

and that the inclusion of the triggering potential of small magnitude events improves forecast performance (*Helmstetter et al.*, 2006). Since our goal is to measure any improvement in the stress-based models, here we implement a standard ETAS version (*Seif et al.*, 2017) to be used as benchmark and we acknowledge that a better performance may be reached by other ETAS formulations.

The ETAS model assumes that: (1) each event produces a population of direct offspring earthquakes (whose abundance depends on the parent's magnitude) that follow an Omori-like decay, (2) seismicity is modelled as a point process that unfolds according to a stochastic branching process, (3) the magnitude of each triggered earthquake can exceed that of its direct parent event. The ETAS earthquake rate (λ) – also called "conditional intensity" – at time t and location (x,y) is conditioned by the past seismicity history (H_t), and is given by

$$\lambda(x, y, t \mid H_t) = \mu(x, y) + \sum_{i:t_i<t} g(t - t_i, x - x_i, y - y_i; M_i), \quad (9)$$

with $\mu(x, y)$ the time-independent Poissonian background event rate and g the kernel that includes the triggering contribution of each earthquake occurred at $t_i < t$. The triggering part is constituted of a productivity term and temporal and spatial probability distribution functions (PDFs) that we express using the standard formulation of *Ogata* (1998):

$$g(t, x, y; M) = K_0 e^{\alpha(M - M_{cut})} \cdot c^{p-1}(t + c)^{-p}(p - 1) \cdot f(x, y|M). \quad (10)$$

The first term in equation (10) governs the earthquake productivity, with M_{cut} a minimum triggering magnitude, K_0 regulates the short-term aftershock production from a parent event with $M \geq M_{cut}$, and α establishes the triggering capabilities of an earthquake as a function of its magnitude. The second term is the normalized temporal distribution of triggered events including the modified Omori-Utsu law (*Utsu*, 1961) parameters. $f(x, y|M)$ is the PDF describing the spatial

decay of the progeny around the parent earthquake given the parent's magnitude. For the latter, we use an isotropic power law distribution (e.g. *Ogata and Zhuang*, 2006; *Werner et al.*, 2011; *Seif et al.*, 2017):

$$f(x,y|M) = \left(d\, e^{\gamma(M-M_{cut})}\right)^{q-1}/\pi \cdot \left(x^2+y^2+d\cdot e^{\gamma(M_i-M_{cut})}\right)^{-q}(q-1), \qquad (11)$$

where q describes the spatial decay of triggered earthquakes, and $d \cdot e^{\gamma(M_i-M_{cut})}$ defines the size of the aftershock zone as a function of the parent event's magnitude (M_i).

We estimate the ETAS parameters (Table S1) in the testing region by means of the Maximum Likelihood Estimation (MLE) method (*Zhuang et al.*, 2012) applied to the 1983-2019 subset of the learning phase catalog. We use the first two years of the learning phase (1981-1982) as auxiliary seismicity to account for event interactions outside the target time window. The fitting process also considers earthquake triggering coming from outside the spatial boundaries of the target region by including the contribution of the M2.5+ seismicity occurred within the entire Southern California Seismic Network (SCSN) authoritative region. We set M_{cut} = 2.5 and $\alpha = \beta = \log(10)\cdot b$ (with Gutenberg-Richter b-value = 1) to improve ETAS' productivity forecasts (*Hainzl et al.*, 2008; *Seif et al.*, 2017; *Zhang et al.*, 2020). We keep the ETAS parameters fixed during the whole 1-month horizon and simulate 1,000 catalogs in each forecast time window (dt).

Results

Here, we present (1) the stress interaction results considering the UCERF3 faults within a ~120 km radius from the mainshocks and (2) the physics-based and statistical forecasts expressed as expected number of events in the whole testing region within 1-day time intervals for a 1-month time horizon.

Coulomb Stress interactions

As a first order picture of coseismic stress perturbations, we estimate Coulomb stress change values on (1) the surfaces of UCERF3 (*Dawson*, 2013) mapped faults and (2) on the Mw 7.1 fault plane using the geometry reported in the USGS finite-fault model. For these calculations, we implement a slightly coarser discretization considering 5-km depth intervals between 0-25 km (Figure 2) and a wide range of friction coefficients (0.2-0.8). The 4 July Mw 6.4 earthquake moment tensor calculation has northwest trending right-lateral, and northeast trending left-lateral solutions. We choose to simulate the left-lateral plane based on observed deformation from InSAR (Figure S1). We conclude that the 4 July Mw 6.4 shock likely triggered the 6 July Mw 7.1 earthquake based on calculated 0.08 to 0.2 MPa stress increases in the area of the Mw 7.1 hypocenter (Figure 2a), with the range depending on assigned friction coefficients. While failure stress at the hypocentral area of the Mw 7.1 shock was increased, the eventual rupture areas around that region had calculated stress decreases between -0.09 to -0.25MPa (Figure 2a). It does not appear that the Mw 7.1 slip distribution was affected by these stress decreases because it shows relatively uniform slip despite the stress change variations (Figure S2). The 4 July Mw 6.4 generally reduced stress or caused very small increases on most nearby surrounding faults (as defined by UCERF3) with the exception of the central Garlock fault, which had a more significant stress increase of 0.03 to 0.07 MPa (Figure 2a).

The combined stress change effects of the 4 July Mw 6.4 and 6 July Mw 7.1 earthquakes are calculated on surrounding UCERF3 faults (Figure 2b). The Garlock fault is the longest fault in the region and is believed by some to have the potential to host the largest earthquakes; the central segment of this fault had a maximum 0.006-0.338 MPa stress increase caused by the combined Mw 6.4 and Mw 7.1 Ridgecrest earthquakes. Significant ($\Delta CFF \geq 0.01$MPa; *Harris and Simpson*,

1992; *Hardebeck et al.*, 1998) stress increases are also noted on the Southern Sierra Nevada Fault (maximum ΔCFF = 0.258 MPa), Owens Valley (0.116 MPa), Tank Canyon (0.090 MPa), Panamint Valley faults (0.048 MPa), Lake Isabella (0.042 MPa) and Blackwater (0.036 MPa) (Table S2).

Earthquake Forecasts

Here, we present the results in terms of (a) time evolution of expected seismicity, (b) spatial maps of M2.5+ expected earthquakes within specific time periods starting after the Mw 6.4 Searles Valley event, for the short (24 hours after the mainshocks), and intermediate-term (1 month) time windows. We also present the model validation for the first month of the Ridgecrest sequence using the S and T-test metrics (*Zechar et al.*, 2010; *Rhoades et al.*, 2011) implemented in the CSEP initiative, which perform a model-data consistency check and an inter-model predictive skill comparison, respectively. All forecast model results are provided in the electronic supplement to this article (Figures S3-S6).

Earthquake Rates Forecast

In Figure 3a we present the M2.5+ observed vs. expected daily occurrences. The preliminary and oversimplified CRS1-*basic* underestimates the seismicity rates by an order of magnitude, which is in agreement with the results from a similar stress-based implementation in other sequences (e.g. *Mancini et al.*, 2019). We observe that the introduction of optimized fault constitutive parameters in CRS2-*optimized* reverses the severe under-prediction of CRS1-*basic,* making all the successive realizations comparable to the real-time catalog. While we find that all the physics-based models match well with the number of M2.5+ events in the 24 hours following

the Mw 6.4 event, they mostly overpredict in the short-term after the Mw 7.1 shock, for a maximum of 120% in CRS2 (1579 M2.5+ expected vs. 713 observed) and a minimum of 26% in CRS7 (899 expected events), with a general good agreement over the entire first month of the sequence. The ETAS model, with rates expressed from the mean of the simulations, strongly overpredicts after both mainshocks. However, we expect the early incompleteness of the real-time catalog following the Ridgecrest main events to affect the apparent overprediction of most of the models.

Figure 3b compares the cumulative number of expected vs. observed earthquakes. We find that (1) the inclusion of secondary triggering effects from CRS4-*secondary* onwards leads to a 15% increase in the cumulative number of forecasted aftershocks during the first month, almost entirely due to the short-term triggering expected from the early Mw 7.1 aftershocks (days 2-3); (2) CRS6-*eFFM*, based on the edited USGS finite-fault model (eFFM), reduces the 24 hours post-mainshock over-prediction; (3) the update of the receivers using the unfolding aftershock rupture parameters (CRS7-*new_FMs*), although appearing not critical immediately after the Ridgecrest mainshock (<1 day) due to the limited number of available early focal mechanisms, brings an important improvement between days 2 and 3 by reducing the overprediction seen in models CRS4/5/6; (4) although ETAS fits the seismicity decay well in the 34-hour window between the main events, it presents the poorest performance immediately after the Mw 7.1 shock; (5) stress-based models fit adequately the seismicity decay from the third day onwards, with model CRS7-*new_FMs* better approximating the total number of events within Poissonian uncertainty.

We finally test how the implementation of a different coefficient of friction in the Coulomb calculations affects the output of the best performing model. When we use μ' values of 0.2 and 0.6, we find a variability of the expected rates after the mainshocks of about ±20% (Figure S3),

388 which reflects the importance of coseismic normal stress changes. Here, we consider a spatially
389 uniform coefficient of friction, such that varying its value does not affect the spatial performance
390 of the forecast. However, the array of faults in the region likely have different apparent friction
391 coefficients, with small, limited offset faults having higher values than more evolved higher slip
392 faults (e.g., *Parsons et al.*, 1999). In an operational forecast setting where it is not possible to assess
393 the frictional state of every fault, an average intermediate value is a reasonable approach for a
394 broad region.
395
396 ***Forecast Maps***
397 Figure 4 shows the seismicity rate maps of the most preliminary (CRS1-*basic*) and the most
398 enhanced (CRS7-*new_FMs*) physics-based forecasts against the statistical ETAS realization for
399 the 24 hours following the Mw 6.4 Searles Valley and the Mw 7.1 Ridgecrest events and for the
400 whole 1-month horizon. Although we formally assess the performance of the models for the entire
401 testing area, in Figure 4 we show the sub-region characterized by the highest aftershock
402 productivity. Similar maps for the complete set of models, including the alternative CRS7-*usgs*,
403 are available as supplemental material to this paper (Figures S4-S6).
404 The expected CRS and ETAS seismicity patterns in the 24 hours following the Mw 6.4 Searles
405 Valley event (Figure S4) mostly miss the observed L-shaped aftershock distribution. The visual
406 comparison between the stress-based models (Figures 4a,d and S4a-h) and ETAS (Figure 4g)
407 shows how both forecasting methods suffer from the lack of a finite-fault model that describes the
408 complex slip distribution along either the NE-SW left-lateral or NW-SE right-lateral fault sections
409 involved. The most striking feature of these maps is the misalignment between the expected vs.
410 observed seismicity along the left-lateral fault (Figure 4a), arising from the selection of the

kinematic parameters assigned to the Mw 6.4 rupture. For the CRS models, including CRS6-*eFFM*, we initially use the real-time catalog of focal mechanisms by the SCEDC where a strike = 69° was reported. However, the USGS strike of 48° better matches visually the distribution of triggered aftershocks along the Mw 6.4 left-lateral and also part of the right-lateral rupture before the Mw 7.1 event (CRS7-*usgs*, Figure S4h). This result highlights the critical role of real-time rupture characterization for operational earthquake forecasting purposes, especially since the uncertainties behind fault strike angles in modern networks reach 20° (*Kagan*, 2003). Figure S4 shows that this misalignment only partially recovers when rates are enhanced by the implementation of optimized rate-and-state variables (CRS2; Figure S4b) and off-fault receiver planes are based on regional faulting styles (CRS3; Figure S4c). The lack of M2.5+ seismicity in the real-time ComCat catalog in the 31 minutes between the Mw 4.0 foreshock and the Mw 6.4 Searles Valley earthquake results in minimal differences in the spatial distribution of expected rates between CRS3 and the remaining stress-based models.

The forecast maps for the first 24 hours after the Mw 7.1 Ridgecrest mainshock (Figure S5) show that: (1) the highly clustered seismicity at the northwestern fault edge is captured even in the preliminary CRS1-*basic* model, although the uniform slip model results in misaligned aftershock distributions (Figure 4b); (2) from CRS2 onwards, seismicity rates increase across the Ridgecrest fault, marking the importance of an optimized rate-and-state parameterization; (3) the finite-fault slip model incorporation leads to high near-source rates in agreement with the distribution of early aftershocks (CRS3, Figure S5c) but also increased rates east of the South Sierra Nevada Fault: the latter likely are an artifact due to the noisy preliminary USGS source model; (4) the early post-mainshock seismicity NW of the Coso Volcanic Field (CVF) is partially underestimated initially (Figure S5, c-d) but recovers when coseismic stresses are resolved on pre-existing ruptures taken

434 from past focal mechanisms (Fig S5e); (5) the edited USGS finite-fault slip model improves the
435 expected patterns east of the South Sierra Nevada Fault and reduces the overestimation in the
436 southern CVF region; (6) the isotropic ETAS model adequately captures the triggered seismicity
437 in the near source, but overpredicts in the off-fault region and underestimates observed rates
438 northwest of the CVF (Figure 4h).

439 The 1-month cumulative maps (Figure S6) illustrate that: (1) the preliminary model suffers
440 from underestimation within stress shadows and the previously described misalignment resulting
441 from the use of the SCEDC preliminary focal mechanism (Figure 4c); (2) the near-source forecast
442 improves when using the finite-fault slip model though in its preliminary non-edited version
443 (CRS3-*FFM/SSI*, Figure S6c) while the visual comparison suggests further local improvements
444 when secondary triggering effects are considered (CRS4-*secondary*, Figure S6d); (3) the small-
445 scale rupture heterogeneity, represented by pre-existing ruptures taken from past focal
446 mechanisms, provides benefits to the off-fault representation (CRS3 vs. CRS5, Figure S6c,e); (4)
447 updating the receiver fault representation to include evolving aftershock planes presents localized
448 differences in expected rates that become also notable on the SE fault termination near the central
449 Garlock Fault (Figure 4f); (5) the ETAS model (Figure 4i) accurately reproduces the high observed
450 rates in the near-source area and around the CVF but, given its basic parameterization that does
451 not incorporate fault information, it projects too wide an aftershock zone that leads to
452 overprediction at intermediate distances.

453 The most advanced CRS7-*new_FMs* model predicts heightened rates on the northern section of
454 South Sierra Nevada (SSN), and less heightened rates on southern Garlock, around the southern
455 Owens Valley, Lake Isabella and White Wolf faults (Figure S7a). We do not predict important
456 triggered seismicity on the Panamint Valley Fault, Tank Canyon and on the southern SSN section.

A common output from all the physics-based forecast models is the increased expected rate along the Central Garlock Fault which is yet to be observed as of the time of writing.

Statistical Evaluation of Model Performance

We quantify the predictive skills of the models by means of two statistical tests currently implemented by the Collaboratory for the Study of Earthquake Predictability. To assess the absolute spatial performance of the forecasts, we use the S-test joint log-likelihood scores (jLL_S; *Zechar et al.*, 2010) for the 24 hours following the two mainshocks and for the 1-month cumulative forecast horizon. We then carry out a comparative analysis of model performance through the T-test metrics (*Rhoades et al.*, 2011) describing the information gains per earthquake (IG) with respect to the simple model CRS1-*basic*. Table 2 summarizes the statistical scores of the physics-based and ETAS models.

We compare the ability of models to reproduce the spatial aftershock patterns by expressing the forecasts in term of cumulative joint log-likelihood vs. time over the entire testing region. Given a forecast λ, we calculate the logarithm of the likelihood (LL) of observing ω earthquakes at each 2x2 km cell of the domain as (*Schorlemmer et al.*, 2007):

$$LL(\omega|\lambda) = \log\big(Pr(\omega|\lambda)\big) = -\lambda + \omega log\lambda - \log(\omega!), \quad (12)$$

where $Pr(\omega|\lambda)$ is the probability of observing ω assuming that λ is correct. The log-likelihoods used in the S-test (LL_S) make use of normalized λ rates in order to isolate the spatial component of the forecasts. By simply summing the LL_S of all the (i, j) cells, we obtain the joint S-test log-likelihood scores (jLL_S):

480 $$jLL_S(\Omega|\Lambda) = \sum_{(i,j)\in R} \left(-\lambda(i,j) + \omega(i,j)\, log\big(\lambda(i,j)\big) - log(\omega(i,j)!)\right), \quad (13)$$

481

482 where Ω and Λ are the observed and forecasted catalogs. Log-likelihoods are negative by
483 definition, with higher values indicating better predictive skills. Figure 5 shows the cumulative
484 temporal evolution of jLL_S. We find that: (1) ETAS and the most enhanced CRS7 achieve the best
485 overall spatial consistency; (2) CRS7-*usgs* presents similar spatial performance to ETAS within
486 the first week of the sequence, with the Mw 6.4 USGS focal mechanism implementation increasing
487 significantly its likelihood score (in the first 24 hours of the experiment, CRS7-*usgs*$_{\text{JLLS}}$ = -599 vs.
488 ETAS$_{\text{JLLS}}$ = -361); (3) stress-based forecasts from CRS5-*past_FMs* onwards outperform the
489 isotropic ETAS model after the Ridgecrest mainshock (Table 2), underscoring the importance of
490 updating the receiver plane representation using past (CRS5) or both past and aftershock focal
491 mechanism planes (CRS7-*new_FMs*); (4) the systematic log-likelihood increase with the growing
492 CRS model complexity illustrates how different components (e.g. the Mw 7.1 slip model,
493 secondary triggering effects, receiver updates) improve the overall model performance.
494 We also find that the implementation of a reference seismicity rate in CRS7-*new_FMs* improves
495 the joint log-likelihood in the 24 hours after the Mw 6.4 event (Figure 7c). However, the score
496 deteriorates following the Mw 7.1 mainshock reaching a slightly worse performance in the
497 intermediate term when compared to the model version implementing a background rate. This
498 result is due to the higher rates projected by the model in zones of high clustering of past triggered
499 seismicity, such as the area of the 1995 Ridgecrest aftershock sequence and the regions within and
500 NE of the Coso field (Figure 7d); in the latter three regions, no significant clustering of M2.5+
501 aftershocks was observed during the first month of the 2019 sequence.

We rank the relative forecast performance using the T-test and information gain (IG) metrics, defined as the average log-likelihood difference per earthquake between a model (A) and a benchmark (B):

$$IG(A,B) = \frac{jLL_A - jLL_B}{N}, \quad (14)$$

where N is the number of observed events. T-test's likelihoods are calculated from unnormalized rates so that both the spatial aftershock distribution and the forecasted seismicity rates influence the score. We calculate the 95% confidence interval over the mean IG from a paired Student's t-test (*Rhoades et al.*, 2011). A positive information gain per earthquake presents an improvement with respect to a benchmark, and we deem the improvement significant if the confidence interval does not enclose zero. In Figure 6 we compare the average daily information gains when CRS1-*basic* is taken as benchmark. The short-term results for the 24 hours after the Mw 6.4 suggest that although all physics-based models are genuinely more informative than CRS1 ($IG_{CRS\text{-}1} \geq 2.5$) none of them except the most enhanced one (CRS7-*usgs*, $IG_{CRS1} = 5.65 \pm 0.49$; grey square in Figure 6a) perform as well as ETAS ($IG_{CRS1} = 6.40 \pm 0.41$). Following the Mw 7.1 Ridgecrest mainshock (Figure 6b) ETAS is outperformed by most of the stress-based forecasts as shown by the low IG values. Here, the decisive factors behind the CRS performance improvement are the edited fault slip model and the receiver updates. We also find a small overall performance improvement ($\Delta IG \approx 0.15$) when receiver planes are updated using the first 34 hours aftershocks (CRS7-*new_FMs*); rupture parameters for this time window are taken from the admittedly limited number of early aftershock focal mechanisms but, as we show further on, this improvement presents a significant spatial component. The cumulative 1-month evaluation window (Figure 6c) reveals similar information gain patterns. Here, CRS7-*new_FMs* outperforms CRS5-*past_FMs* highlighting the

medium-term effect of receiver plane updates within the evolving sequence. Finally, the enhanced physics-based model CRS7-*usgs* achieves a higher mean average information gain per earthquake than ETAS.

By plotting the log-likelihood differences in the space domain (Figure S8), we observe that the fault-based CRS forecasts are more localized along the ruptures when compared to the standard ETAS model and outperform the statistical counterpart in the broader region by predicting low off-fault rates (Figure S8b). However, if we look at smaller distances, we notice that the ETAS model is more robust on the strictly near-fault area (Figure S8c) in agreement with similar previous experiments (e.g. *Segou et al.*, 2013; *Mancini et al*., 2019), although the enhanced physics-based model CRS7-*usgs* significantly outperforms ETAS in the region of high aftershock clustering around the north-western edge of the Ridgecrest rupture.

To better evaluate the effect of updating the receiver planes during the unfolding aftershock sequence, we show in Figure 7a the T-test's log-likelihood differences the for the 1-month forecast between CRS6, updated by past focal mechanisms, and CRS7, updated by past and evolving focal mechanisms. We see two regions characterized by a clear performance improvement (green cells) arising within an otherwise noisy ΔLL signal. We exclude from this discussion the wider area of the Coso field since triggering mechanisms within this active volcanic region may be influenced by other phenomena (e.g. fluid flow; *Martinez-Garzón et al*., 2018). In Figure 7b-d, we plot the distributions of pre- and post-Ridgecrest focal mechanisms in the identified regions using the ternary diagrams of *Frohlich and Apperson* (1992), with the addition of a third zone of interest close to the Garlock Fault characterized by lower aftershock rates and mostly unvaried CRS model performance. To facilitate our interpretation, we present focal mechanisms of cells with notable cumulative log-likelihood difference $|\Delta LL| \geq 6$. In the southern-edge zone, the significance behind

548 the update using evolving focal mechanisms (Figure 7d) is smaller since the pre- and post-
549 Ridgecrest focal mechanism populations remains similar. However, the results suggest a shift
550 between pre- and post-Ridgecrest focal mechanism distributions in the two areas (Zone 1 and 2;
551 Figure 7b-c) where the receivers update with evolving aftershocks leads to a robust improvement,
552 with promoted strike-slip ruptures (from 54% to 69% and from 53% to 67% in zones 1 and 2,
553 respectively) and suppressed normal fault aftershocks (from 25% to 10% and from 24% to 13%).
554 To determine whether the pre-existing normal faulting (pre-Ridgecrest) is in fact discouraged
555 within the evolving sequence, we resolve the Ridgecrest coseismic stress changes on the average
556 plane of the pre-Ridgecrest normal focal mechanisms (Figure S9). Indeed, we find that the ΔCFF
557 estimates support a near source stress shadow on pre-existing normal faults that is more evident
558 between 2-12 km depth in Zone 2 (Figure S9, b-f) and below 4 km in Zone 1 (Figure S9 c-f). The
559 latter observation provides a physical basis for the shift in the focal mechanism population during
560 the unfolding Ridgecrest sequence but also points out the importance of forecast updates using
561 aftershock data.
562

563 ## Discussion and Conclusions

564 We tested the predictive skills of seven Coulomb rate-and-state (CRS) forecasts developed
565 within a pseudo-prospective experiment covering the first month of the 2019 Ridgecrest sequence.
566 Our models progressively evolve in their implementation: from an over-simplified
567 parameterization, based on uniform slip representation and parallel receiver faults, to the most
568 complex physical model incorporating optimized rate-and-state fault constitutive parameters,
569 secondary triggering effects, the USGS Mw 7.1 finite-fault slip model and receivers that consider
570 the UCERF3 faults, off-fault rupture patterns based on pre-existing ruptures, and finally near-

source rupture planes revealed by unfolding aftershocks. The forecast results suggest high expected rates along the whole ~75 km long near-fault region, as confirmed by the observed events. All physics-based models expect increased seismicity rates in Central Garlock Fault, though not significant reactivation has occurred at the time of this writing other than the observed triggered creep (*Barnhart et al.*, 2019). However, delayed aftershocks may be expected on low-stressing rate faults, which highlights the challenges that short- and long-term forecasts must address (*Toda and Stein*, 2018).

When we validate models by means of the formal statistical tests currently implemented within the CSEP community (*Zechar et al.*, 2010; *Rhoades et al.*, 2011), we see that our results agree with recent works suggesting that advances in the implementation of short-term physics-based earthquake forecasting (e.g. *Segou and Parsons*, 2016) show significant performance increases and can approach, or at times outperform, simple benchmark ETAS models. Specifically, our results confirm those of previous forecast experiments suggesting that critical components such as finite-fault rupture models, secondary triggering effects, optimized rate-and-state parameters and spatially variable receiver faults significantly enhance the predictive skills of Coulomb stress-based models (*Cattania et al.*, 2018; *Mancini et al.*, 2019). Our conclusions are further supported by recent modelling developments that illustrate the importance of past focal mechanism data in the estimation of aftershock rupture styles (*Segou and Parsons*, 2020).

Importantly, in this study we evaluated the significance of updating critical components of physics-based models, such as the receiver planes, using aftershock data from the unfolding Ridgecrest sequence. The observed evolving spatial and temporal diversity between the pre-Ridgecrest and within-sequence focal mechanism populations offers a physical interpretation for the estimated local performance improvement, reflected in higher information gains in different

regions across the fault. We document a shift in the faulting styles of local triggered seismicity illustrated by a decrease in the percentage of normal fault earthquakes (~25% pre-Ridgecrest vs. ~10% within the aftershock sequence). In that context, earthquakes on specific pre-existing faulting styles at a local fine scale might be suppressed while others may be enhanced. Therefore, updating the modelled source and receiver populations as aftershock data unfolds is an important step for improving the performance of short-term stress-based earthquake forecasts.

On the other hand, our experimental design showcases one of the modelling caveats that currently affect physics-based aftershock forecasts. We clearly see how, even in a data-rich environment for real-time earthquake products such as California, uncertainties of early focal mechanisms and slip models can be detrimental for operational stress-based forecast models. In particular, the variability of the kinematic parameters associated to the Mw 6.4 Searles Valley event from different providers reveals the influence of data choices among multiple authoritative sources. However, it is extremely encouraging that, although subject to assumptions regarding epistemic and aleatory uncertainties, the most enhanced CRS models that make use of aftershock data can generate informative forecasts that are beginning to compare well to those of statistical models.

Data and resources

Some data used in this study were collected by the California Institute of Technology (Caltech) and U.S. Geological Survey (USGS) Southern California Seismic Network (https://doi:10.7914/SN/CI) and distributed by the Southern California Earthquake Data Center (SCEDC). The *Hauksson et al.* (2012) and *Yang et al.* (2012) catalogs of seismicity and focal mechanisms can be acquired through access to the SCEDC website

(https://scedc.caltech.edu/research-tools/altcatalogs.html), as well as the catalog of focal mechanisms for the Ridgecrest sequence (https://service.scedc.caltech.edu/eq-catalogs/FMsearch.php). The ANSS Comprehensive Earthquake Catalog (ComCat) can be searched at https://earthquake.usgs.gov/earthquakes/search/. The stress inversion by *Luttrell and Smith-Konter* (2017) is available on the SCEC Community Stress Model webpage (https://www.scec.org/research/csm). The preliminary slip model by G. P. Hayes (USGS) for the Mw 7.1 Ridgecrest mainshock is available at the USGS event webpage: https://earthquake.usgs.gov/earthquakes/eventpage/ci38457511/finite-fault. UCERF3 fault section data is accessible through the open-file report at http://pubs.usgs.gov/of/2013/1165/pdf/ofr2013-1165_appendixC.pdf.

The code 'CRS' (*Cattania and Khalid*, 2016) can be downloaded at https://github.com/camcat/crs. Coseismic stress change on 3D individual UCERF3 faults are calculated using Coulomb 3.3 (*Toda et al., 2*011; https://earthquake.usgs.gov/research/software/coulomb/) and the software 'DLC' by R. Simpson (USGS) based on the subroutines of *Okada* (1992). The supplemental material attached to this manuscript provides the full set of forecast maps, model testing results, and static stress changes calculations.

Acknowledgments

The authors would like to thank the Editor-in-Chief Thomas Pratt, the Guest Editor Zachary E. Ross and two anonymous reviewers for the thorough and insightful comments that helped us improving the manuscript.

S. Mancini is supported by a NERC GW4+ Doctoral Training Partnership studentship from the Natural Environment Research Council (NE/L002434/1) and by the BGS University Funding

Initiative Ph.D. studentship (S350). This project (M.J.W.) has received funding from the European Union's Horizon 2020 research and innovation program under grant agreement No 821115, Real-Time Earthquake Risk Reduction for a Resilient Europe (RISE) and (M.S.) from the NERC-NSFGEO funded project 'The Central Apennines Earthquake Cascade Under a New Microscope' (NE/R0000794/1). This research was also supported by the Southern California Earthquake Center (Contribution No. 10017). SCEC is funded by NSF Cooperative Agreement EAR-1600087 & USGS Cooperative Agreement G17AC00047.

References

Barnhart, W. D., G. P. Hayes, and R. D. Gold (2019). The July 2019 Ridgecrest, California, earthquake sequence: Kinematics of slip and stressing in cross-fault ruptures, *Geophys. Res. Lett.* 46. https://doi.org/10.1029/2019GL084741

Bryant, W.A., compiler, 2017, Fault number 72, Little Lake fault zone, in Quaternary fault and fold database of the United States: U.S. Geological Survey website, https://earthquakes.usgs.gov/hazards/qfaults

Cattania, C., and F. Khalid (2016). A parallel code to calculate rate-state seismicity evolution induced by time dependent, heterogeneous Coulomb stress changes, *Computers & Geosciences* 94, 48-55.

Cattania, C., M. J. Werner, W. Marzocchi, S. Hainzl, D. Rhoades, M. Gerstenberger, M. Liukis, W. Savran, A. Christophersen, A. Helmstetter, A. Jimenez et al. (2018). The Forecasting Skill of Physics-Based Seismicity Models during the 2010–2012 Canterbury, New Zealand, Earthquake Sequence. *Seismol. Res. Lett.* 89(4), 1238–1250. https://doi.org/10.1785/0220180033.

Chen, K. H., R. Bürgmann, and R. M. M. Nadeau (2013). Do earthquakes talk to each other? Triggering and interaction of repeating sequences at Parkfield, *J. Geophys. Res. Solid Earth* 118, 165–182, https://doi.org/10.1029/2012JB009486.

Chen, K., J. Avouac, S. Aati, C. Milliner, F. Zheng, and C. Shi (2020). Cascading and pulse-like ruptures during the 2019 Ridgecrest earthquakes in the Eastern California Shear Zone, *Nat. Comm.* 11, 22. https://doi.org/10.1038/s41467-019-13750-w.

Dawson, T. E. (2013). Appendix A – Updates to the California Reference Fault Parameter Database – Uniform California Earthquake Rupture Forecast, Version 3 Fault Models 3.1 and 3.2, U.S. Geological Survey Open-File Report, 2013–1165, 18 p., http://pubs.usgs.gov/of/2013/1165/pdf/ofr2013-1165_appendixC.pdf

Dieterich, J. H. (1994). A constitutive law for rate of earthquake production and its application to earthquake clustering, *J. Geophys. Res.*, 99(B2), 2601–2618.

Dieterich, J. H., V. Cayol, and P. Okubo (2000). The use of earthquake rate changes as stress meter at Kilauea volcano, *Nature.*, 408, 457–460.

Field, E. H., K. R. Milner, J. L. Hardebeck, M. T. Page, N. van der Elst, T. H. Jordan, A. J. Michael, B. E. Shaw, and M. J. Werner (2017). A spatiotemporal clustering model for the third Uniform California Earthquake Rupture Forecast (UCERF3-ETAS): toward an operational earthquake forecast, *Bull. Seismol. Soc. Am.* 107(3), 1049-1081. https://doi.org/10.1785/0120160173.

Frohlich, C., and K. Apperson (1992). Earthquake focal mechanisms, moment tensors, and the consistency of seismic activity near plate boundaries, *Tectonics* 11(2), 279-296.

Gerstenberger, M. C., and D. A. Rhoades (2010). New Zealand earthquake forecast testing centre, *Pure Appl. Geophys.* 167, 8-9. 877-892. https://doi.org/10.1007/s00024-010-0082-4.

Guy, M., J. Patton, J. Fee, M. Hearne, E. Martinez, D. Ketchum. C. Worden, V. Quitoriano, E. Hunter, G. Smoczyk et al. (2015). National Earthquake Information Center systems overview and integration (USGS numbered series No. 2015–1120), Open-File Report. U.S. Geological Survey, Reston, VA.

690 Hainzl, S., A. Christophersen, and B. Enescu (2008). Impact of earthquake rupture extension on
691 parameters estimations of point-process models, *Bull. Seismol. Soc. Am.* 98(4), 2066-2072.
692 https://doi.org/10.1785/0120070256.

693 Hainzl, S., O. Zakharova, and D. Marsan (2013). Impact of aseismic transients on the estimation
694 of aftershock productivity parameters, *Bull. Seismol. Soc. Am.* 103, 1723–1732.

695 Hanks, T., and H. Kanamori (1979). A moment magnitude scale, *J. Geophys. Res.* 84, 2348–2350.
696 https://doi.org/10.1029/JB084iB05p02348.

697 Hardebeck, J. L., J. J. Nazareth, and E. Hauksson (1998). The static stress change triggering model:
698 Constraints from two southern California earthquake sequences, *J. Geophys. Res.*, 103, 24427-
699 24437.

700 Harris, R. A., and R. W. Simpson (1992). Changes in static stress on southern California faults
701 after the 1992 Landers earthquake, *Nature* 360(6401), 251–254.

702 Hauksson, E., K. Hutton, H. Kanamori, L. Jones, J. Mori, S. E. Hough, and G. Roquemore (1995).
703 Preliminary report on the 1995 Ridgecrest earthquake sequence in Eastern California, *Seismol.*
704 *Res. Lett.*, 66(6), 54-60.

705 Hauksson, E., W. Yang, and P. M. Shearer (2012). Waveform relocated earthquake catalog for
706 southern California (1981 to 2011). *Bull. Seismol. Soc. Am.* 102(5), 2,239–2,244.

707 Heimisson, E. R., and P. Segall (2018). Constitutive law for earthquake production based on rate-
708 and- state friction: Dieterich 1994 revisited. *J. Geophys. Res. Solid Earth* 123, 4141- 4156.
709 https://doi.org/10.1029/2018JB015656.

710 Heimisson, E. R. (2019). Constitutive law for earthquake production based on rate-and- state
711 friction: Theory and Application of Interacting Sources. *J. Geophys. Res. Solid Earth* 124,
712 1802- 1821. https://doi.org/10.1029/2018JB016823.

713 Helmstetter, A., Y. Y. Kagan, and D. D. Jackson (2005). Importance of small earthquakes for
714 stress transfers and earthquake triggering, *J. Geophys. Res.* 110.
715 https://doi.org/10.1029/2004JB003286.

716 Helmstetter, A., Y. Kagan, and D. D. Jackson (2006). Comparison of short-term and time-
717 independent earthquake forecast models for Southern California, *Bull. Seismol. Soc. Am*. 96(1),
718 90–106. https://doi.org/10.1785/0120050067.

719 Helmstetter, A., Kagan, Y., & Jackson, D. D. (2007). High-resolution Time-independent Grid-
720 based Forecast for M >= 5 Earthquakes in California. *Seismol. Res. Lett.*, 78(1), 78-86.
721 https://doi.org/10.1785/gssrl.78.1.78.

722 Jordan, T. H. (2006). Earthquake Predictability, Brick by Brick, *Seismol. Res. Lett.* 77(1), 3–6.
723 https://doi.org/10.1785/gssrl.77.1.3.

724 Jordan, T. H., Y. Chen, and I. Main (2011). Operational earthquake forecasting: State of
725 knowledge and guidelines for utilization, *Ann. Geophys.* 54, no. 4. https://doi.org/10.4401/ag-
726 5350.

727 Jordan, T. H., W. Marzocchi, A. J. Michael, and M. C. Gerstenberger (2014). Operational
728 Earthquake Forecasting Can Enhance Earthquake Preparedness, *Seismol. Res. Lett.* 85(5), 955–
729 959. https://doi.org/10.1785/0220140143.

730 Kagan, Y. Y. (2003). Accuracy of modern global earthquake catalogs, *Phys. Earth Planet. In.* 135,
731 173–209.

732 Linker, M. F., and J. H. Dieterich (1992). Effects of variable normal stress on rock friction:
733 Observations and constitutive equations, *J. Geophys. Res.*, 97(92), 4923-4940.
734 https://doi.org/10.1029/92JB00017

735 Luttrell, K., and B. Smith-Konter (2017). Limits on crustal differential stress in southern California
736 from topography and earthquake focal mechanisms, *Geophys. J. Int.* 211, 472–482.
737 https://doi.org/10.1093/gji/ggx301.

738 Mancini, S., M. Segou, M. J. Werner, and C. Cattania (2019). Improving physics-based aftershock
739 forecasts during the 2016-2017 Central Italy earthquake cascade, *J. Geophys. Res. Solid Earth*
740 124. https://doi.org/10.1029/2019JB017874.

741 Martinez-Garzón, P., I. Zaliapin, Y. Ben-Zion, G. Kwiatek, and M. Bohnhoff (2018). Comparative
742 study of earthquake clustering in relation to hydraulic activities at geothermal fields in
743 California, *J. Geophys. Res.* 123, 4041-4062.

744 Marzocchi W., A. M. Lombardi, and E. Casarotti (2014). The establishment of an operational
745 earthquake forecasting system in Italy, *Seismol. Res. Lett.* 85(5), 961-969.

746 Michael, A. J., and M. J. Werner (2018). Preface to the Focus Section on the Collaboratory for the
747 Study of Earthquake Predictability (CSEP): New Results and Future Directions, *Seismol. Res.*
748 *Lett.* 89(4), 1226-1228. https://doi.org/10.1785/0220180161.

749 Mousavi, M., W. Zhu, Y. Sheng, and G. Beroza (2019). CRED: a deep residual network of
750 convolutional and recurrent units for earthquake signal detection, *Sci. Rep.* 9, 10267.
751 https://doi.org/10.1038/s41598-019-45748-1.

752 Okada, Y. (1992). Internal deformation due to shear and tensile faults in a half-space, *Bull.*
753 *Seismol. Soc. Am.* 82, 1018-1040.

754 Ogata, Y. (1988). Statistical models for earthquake occurrences and residual analysis for point
755 processes, *J. Am. Stat. Assoc.* 83(401), 9–27.

756 Ogata, Y. (1998). Space-time point-process models for earthquake occurrences, *Ann. Inst. Stat.*
757 *Math.* 50(2), 379–402. https://doi.org/10.1023/A:1003403601725.

758 Ogata, Y., and J. Zhuang (2006). Space-time ETAS models and an improved extension,
759 *Tectonophysics* 413(1–2), 13–23.

760 Omi T., Y. Ogata, K. Shiomi, B. Enescu, K. Sawazaki, and K. Aihara (2019). Implementation of
761 a real-time system for automatic aftershock forecasting in Japan, *Seismol. Res. Lett.* 90(1), 242-
762 250. https://doi.org//10.1785/0220180213.

763 Parsons, T., R. S. Stein, R. W. Simpson, and P. A. Reasenberg (1999). Stress sensitivity of fault
764 seismicity: a comparison between limited-offset oblique and major strike-slip faults, *J.*
765 *Geophys. Res.* 104, 20183-20202.

766 Rice, J. R. (1992). Fault stress states, pore pressure distributions, and the weakness of the San
767 Andreas Fault, in *Fault mechanics and transport properties of rocks; a festschrift in honour of*
768 *W. F. Brace*, edited by B. Evans and T. Wong, Academic Press, San Diego, CA, USA., 475-
769 503.

770 Rhoades, D. A., D. Schorlemmer, M. C. Gerstenberger, A. Christophersen, J. D. Zechar, and M.
771 Imoto (2011). Efficient testing of earthquake forecasting models, *Acta Geophysica* 59(4), 728–
772 747. https://doi.org/10.2478/s11600-011-0013-5.

773 Ross, Z., M. A. Meier, and E. Hauksson (2018). P wave arrival picking and first-motion polarity
774 determination with deep learning, *J. Geophys. Res. Solid Earth* 122, 5120-5129.
775 https://doi.org/10.1029/2017JB015251.

776 Ross, Z., B. Idini, Z. Jia, O. L. Stephenson, M. Zhong, Z. Wang, Z. Zhan, M. Simons, E. J. Fielding,
777 S. Yun, E. Hauksson et al. (2019). Hierarchical interlocked orthogonal faulting in the 2019
778 Ridgecrest earthquake sequence, *Science* 366, 346-351.

779 Schorlemmer, D., M. C. Gerstenberger, S. Wiemer, D. D. Jackson, and D. A. Rhoades (2007).
780 Earthquake likelihood model testing, *Seismol. Res. Lett.* 78(1), 17–29.
781 https://doi.org/doi:10.1785/gssrl.78.1.17.

782 Segou, M., T. Parsons, and W. Ellsworth (2013). Comparative evaluation of physics-based and
783 statistical forecasts in Northern California, *J. Geophys. Res. Solid Earth* 118, 6219–6240.
784 https://doi.org/10.1002/2013JB010313.

785 Segou, M., and T. Parsons (2016). Prospective Earthquake Forecasts at the Himalayan Front after
786 the 25 April 2015 M 7.8 Gorkha Mainshock, *Seismol. Res. Lett.* 87(4),
787 https://doi.org/10.1785/0220150195.

788 Segou, M., and T. Parsons (2020). A New Technique to Calculate Earthquake Stress Transfer and
789 to Probe the Physics of Aftrshocks, *Bull. Seismol. Soc. Am.* 110(2), 863–873,
790 https://doi.org/10.1785/0120190033.

Seif, S., A. Mignan, J. D. Zechar, M. J. Werner, and S. Wiemer (2017). Estimating ETAS: The effects of truncation, missing data, and model assumptions, *J. Geophys. Res. Solid Earth* 121, 449–469. https://doi.org/10.1002/2016JB012809.

Toda, S., R. S. Stein, K. Richards-Dinger, and B. S. Bozkurt. (2005). Forecasting the evolution of seismicity in southern California: Animations built on earthquake stress transfer, *J. Geophys. Res.* 110, B05S16, https://doi.org/10.1029/2004JB003415.

Toda, S., R. S. Stein, V. Sevilgen, and J. Lin (2011). Coulomb 3.3 Graphic-rich deformation and stress-change software for earthquake, tectonic, and volcano research and teaching – user guide: U.S. Geological Survey Open-File Report 2011-1060, 63 p., http://pubs.usgs.gov/of/2011/1060/.

Toda, S., and R. S. Stein (2018). Why aftershock duration matters for probabilistic seismic hazard assessment, *Bull. Seismol. Soc. Am.* 108(3A), 1414-1426. https://doi.org/10.1785/0120170270.

Utsu, T. (1961). A statistical study on the occurrence of aftershocks, *Geophys. Mag.* 30, 521-605.

Wells, D. L., and K. J. Coppersmith (1994). New empirical relationships among magnitude, rupture length, rupture width, rupture area, and surface displacement, *Bull. Seismol. Soc. Am.* 84, 974–1002.

Werner, M. J., A. Helmstetter, D. D. Jackson, and Y.Y. Kagan (2011), High-resolution long-term and short-term earthquake forecasts for California, *Bull. Seismol. Soc. Am.* 101(4), 1630–1648. https://doi.org/doi:10.1785/01200900.

Yang, W., E. Hauksson, and P. M. Shearer (2012). Computing a large refined catalog of focal mechanisms for southern California (1981–2010): Temporal stability of the style of faulting. *Bull. Seismol. Soc. Am.* 102(3), 1179–1194.

Zechar, J. D., M. C. Gerstenberger, and D. A. Rhoades (2010). Likelihood based tests for evaluating space-rate-magnitude earthquake forecasts, *Bull. Seismol. Soc. Am.* 100, 1184–1195. https://doi.org/10.1785/0120090192.

Zhang, L., M. J. Werner, and K. Goda (2020). Variability of ETAS Parameters in Global Subduction Zones and Applications to Mainshock–Aftershock Hazard Assessment, *Bull. Seismol. Soc. Am.* 110(1), 191–212, https://doi.org/10.1785/0120190121.

Zhuang, J., Y. Ogata, and D. Vere-Jones (2002). Stochastic declustering of space-time earthquake occurrences. *J. Am. Stat. Assoc.* 97(458), 369–380. https://doi.org/10.1198/016214502760046925.

Zhuang, J., D. Harte, M. J. Werner, S. Hainzl, and S. Zhou. (2012). Basic models of Seismicity: Temporal Models, *Community Online Resource for Statistical Seismicity Analysis*. https://doi.org/10.5078/corssa-79905851.

Addresses of authors

Simone Mancini (simone.mancini@bristol.ac.uk), School of Earth Sciences, University of Bristol, BS8 1RL Bristol, UK

Margarita Segou (msegou@bgs.ac.uk), British Geological Survey, The Lyell Center, Research Avenue South, EH14 4AP, Edinburgh, UK

Maximilian Jonas Werner (max.werner@bristol.ac.uk), School of Earth Sciences, University of Bristol, BS8 1RL Bristol, UK

Tom Parsons (tparsons@usgs.gov), United States Geological Survey, USGS P.O. Box 158, Moffett Field, CA 94035, USA

List of Figure Captions

Figure 1. Testing region map. Earthquakes with M2.5+ are shown: pre-Ridgecrest (1981-2019, grey circles), post Mw 6.4 Searles Valley event (orange), post Mw 7.1 Ridgecrest mainshock (red). We report the focal mechanisms of the two mainshocks. The 1 October 1982 Indian Wells event (M=5.2) is indicated as a green triangle. Light blue squares represent the epicenters of the 1995-1996 Ridgecrest sequence mainshocks (M=5.4, 17 August 1995; M=5.8, 20 September 1995; M=5.2, 7 January 1996). The 1995 Ridgecrest sequence activated a number of normal, left and right-lateral faults. Black solid lines indicate the UCERF3 (*Dawson*, 2013) fault traces.

Figure 2. Example of calculated combined coseismic stress changes on mapped UCERF3 faults following (a) the 4 July 2019 Mw 6.4 event and (b) both the Mw 6.4 and 6 July Mw 7.1 earthquakes near Ridgecrest, CA. Hypocenters of the Mw 6.4 and Mw 7.1 earthquakes are shown by yellow stars. Displayed stress changes were calculated using a friction coefficient of 0.4. Stress increases ($\Delta CFF \geq 0.01$ MPa) are calculated on the Central Garlock, South Sierra Nevada, Owens Valley, Tank Canyon, and Panamint Valley faults (Table S2).

Figure 3. Forecast time series for physics-based and statistical models for the first month of the Ridgecrest sequence. (a) Incremental time series: black triangles indicate the observed number of M2.5+ events, while squares represent the expected numbers. (b) Comparison between the cumulative expected vs. observed (black line) rates. The shaded areas indicate Poissonian uncertainties.

Figure 4. Maps of expected seismicity rates for CRS1/7 and ETAS in the area of main aftershock productivity for the first 24 hours following the two mainshocks and for the first month of the Ridgecrest sequence. Observed events (M2.5+) in each time window are represented as circles. The dashed-line square indicates the area of the Coso volcanic field (CVF). S = sources (minimum magnitude); Opt RS = optimized rate-and-state parameters, USD = uniform slip distribution; SUP = spatially uniform receiver planes; SVP = spatially variable planes; eFFM = edited finite-fault slip model; I = isotropic stress field. Aσ values are in MPa, $\dot{\tau}$ values are in MPa/year.

Figure 5. Cumulative S-test joint log-likelihood (jLL_S) timeseries. The scores are obtained by summing the S-test log-likelihoods (LL_S) of each spatial cell and 1-day time step. The vertical dashed line marks the occurrence of the Ridgecrest mainshock.

Figure 6. Average daily information gain per earthquake from the preliminary CRS1-*basic* model for: (a) 24 hour after the Mw 6.4 Searles Valley event, (b) 24 hour after the Mw 7.1 Ridgecrest mainshock and (c) for a cumulative 1-month forecast horizon. The filled grey squares indicate the information gain score of the alternative CRS7-*usgs* model. The horizontal lines mark the no-gain level.

882 **Figure 7.** Influence of pre-existing and evolving rupture populations in stress-based forecasts. (a)
883 Map of cumulative ΔLL for the 1-month forecast horizon between CRS6-*eFFM* and CRS7-
884 *new_FMs*. Positive (green) values indicate a better performance of CRS7-*new_FMs*. Black points
885 indicate the locations of M2.5+ aftershocks between 4 July 2019 and 4 August 2019, while white
886 stars represent the two mainshocks. Values are saturated at ±30 to facilitate visualization. (b-d)
887 Ternary diagrams showing the distribution of focal mechanisms during the pre-sequence (1981-
888 2019, magenta circles) and post-Ridgecrest (blue crosses) time windows.

889

890 **Table 1.** Main features of CRS models.
891

Model	Stress Calculations					Rate-and-state Parameters			
	M_{min}	Secondary Triggering	Slip Distribution	μ'	Receivers	r_0 (1981-2019)	$A\sigma$ (MPa)	$\dot{\tau}$ (MPa/year)	LL optimization
CRS1-*basic*	6.4	No	USD	0.4	SUP	He	0.05	0.0018	No
CRS2-*optimized*	6.4	No	USD	0.4	SUP	He	0.015	0.00025	Yes
CRS3-*FFM/SSI*	6.4	No	FFM (M ≥ 7) USD (M ≥ 6)	0.4	SVP (UCERF3 + SSI)	He	0.02	0.00027	Yes
CRS4-*secondary*	2.5	Yes	FFM (M ≥ 7) USD (M ≥ 2.5) I (M ≥ 2.5)	0.4	SVP (UCERF3 + SSI)	He	0.02	0.00027	Yes
CRS5-*past_FMs*	2.5	Yes	FFM (M ≥ 7) USD (M ≥ 2.5) I (M ≥ 2.5)	0.4	SVP (UCERF3 + SSI + past FMs)	He	0.02	0.00027	Yes
CRS6-*eFFM*	2.5	Yes	eFFM (M ≥ 7) USD (M ≥ 2.5) I (M ≥ 2.5)	0.4	SVP (UCERF3 + SSI + past FMs)	He	0.02	0.00027	Yes
CRS7-*new_FMs*	2.5	Yes	eFFM (M ≥ 7) USD (M ≥ 2.5) I (M ≥ 2.5)	0.4	SVP (UCERF3 + SSI + updating FMs)	He	0.02	0.00027	Yes
CRS7-*usgs*	2.5	Yes	eFFM (M ≥ 7) USGS-USD (M ≥ 2.5) I (M ≥ 2.5)	0.4	SVP (UCERF3 + SSI + updating FMs)	He	0.02	0.00027	Yes

892
893 M_{min} = minimum magnitude for stress sources; FM = focal mechanism; USD = uniform slip
894 distribution; FFM = finite-fault slip model; eFFM = edited finite-fault slip model; I = isotropic
895 stress field; SUP = spatially uniform receiver planes; SVP = spatially variable planes; SSI =
896 smoothed stress inversion; He = heterogeneous.
897

898

899

900

Table 2. Summary of short-term (24 hours) and intermediate-term (1 month) model performance.

Model	24 hours after Mw 6.4			24 hours after Mw 7.1			1 month (cumulative)		
	jLL_S	$N_{F/O}$	IG_{CRS1}	jLL_S	$N_{F/O}$	IG_{CRS1}	jLL_S	$N_{F/O}$	IG_{CRS1}
CRS1-*basic*	-1378	0.10	-	-2905	0.27	-	-8849	0.20	-
CRS2-*optimized*	-1129	0.64	2.55	-3310	2.21	-0.42	-9451	1.46	0.28
CRS3-*FFM/SSI*	-1538	0.91	2.71	-2076	1.77	1.53	-8404	1.22	1.19
CRS4-*secondary*	-1071	0.92	2.92	-2046	1.77	1.57	-7784	1.40	1.34
CRS5-*past_FMs*	-1054	0.94	3.01	-1796	1.94	1.84	-7003	1.46	1.70
CRS6-*eFFM*	-1054	0.94	3.01	-1566	1.39	2.38	-6760	1.17	1.98
CRS7-*new_FMs*	-1054	0.94	3.01	-1482	1.26	2.55	-6440	0.94	2.25
CRS7-*usgs*	-599	0.62	5.65	-1627	1.28	3.35	-6146	0.92	2.50
ETAS	-361	1.75	6.41	-1982	2.61	1.22	-5699	1.98	2.32

jLL_S = S-test joint log-likelihood; $N_{F/O}$ = forecasted/observed event ratio; IG_{CRS1} = information gain on CRS1-*basic*.

920 **Figures with captions**

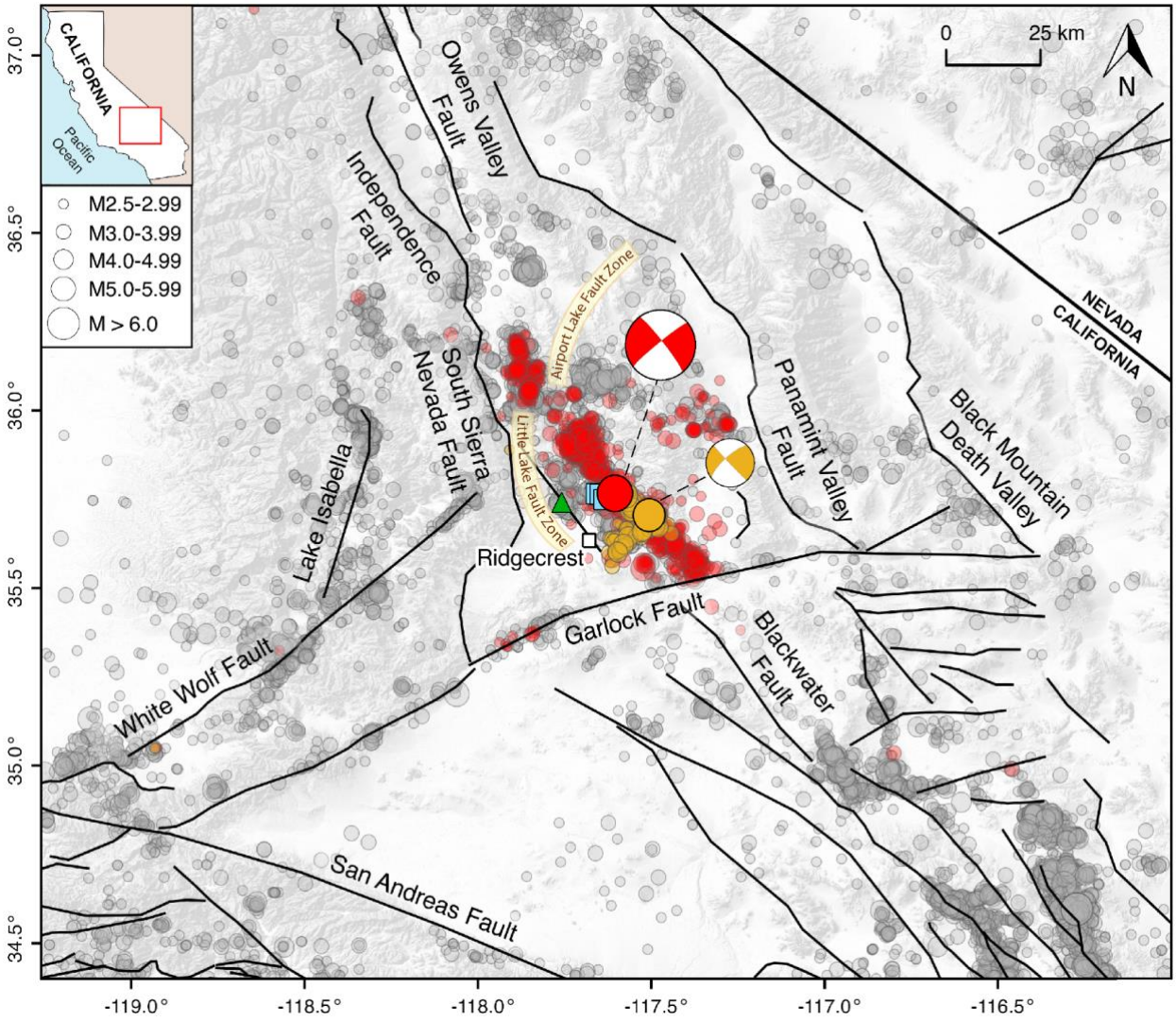

921
922 **Figure 1.** Testing region map. Earthquakes with M2.5+ are shown: pre-Ridgecrest (1981-2019,
923 grey circles), post Mw 6.4 Searles Valley event (orange), post Mw 7.1 Ridgecrest mainshock (red).
924 We report the focal mechanisms of the two mainshocks. The 1 October 1982 Indian Wells event
925 (M=5.2) is indicated as a green triangle. Light blue squares represent the epicenters of the 1995-
926 1996 Ridgecrest sequence mainshocks (M=5.4, 17 August 1995; M=5.8, 20 September 1995;
927 M=5.2, 7 January 1996). The 1995 Ridgecrest sequence activated a number of normal, left and
928 right-lateral faults. Black solid lines indicate the UCERF3 (*Dawson*, 2013) fault traces.
929
930
931
932
933

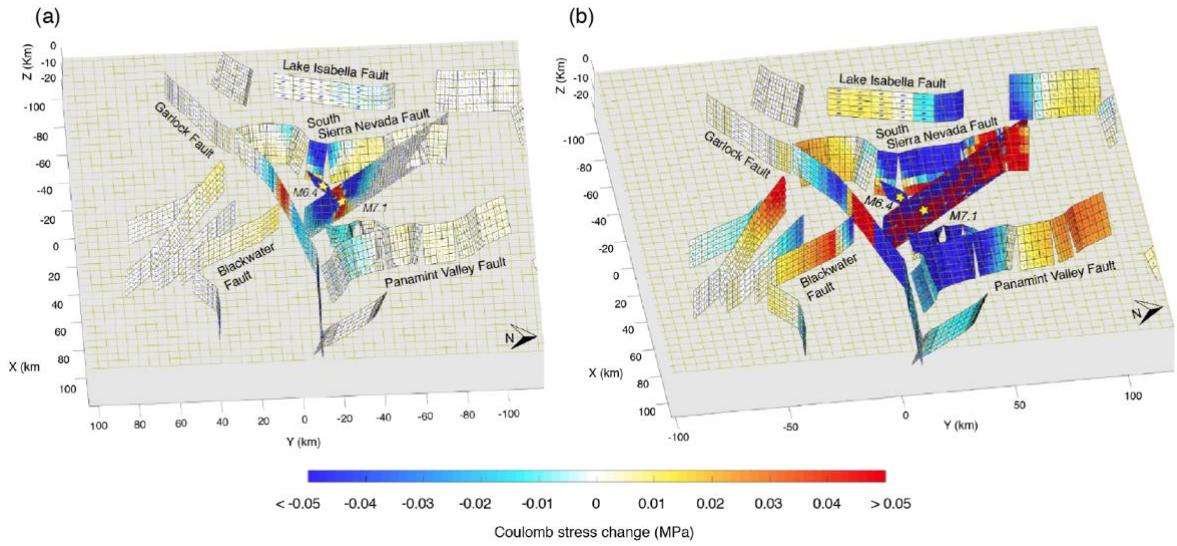

Figure 2. Example of calculated combined coseismic stress changes on mapped UCERF3 faults following (a) the 4 July 2019 Mw 6.4 event and (b) both the Mw 6.4 and 6 July Mw 7.1 earthquakes near Ridgecrest, CA. Hypocenters of the Mw 6.4 and Mw 7.1 earthquakes are shown by yellow stars. Displayed stress changes were calculated using a friction coefficient of 0.4. Stress increases ($\Delta CFF \geq 0.01$ MPa) are calculated on the Central Garlock, South Sierra Nevada, Owens Valley, Tank Canyon, and Panamint Valley faults (Table S2).

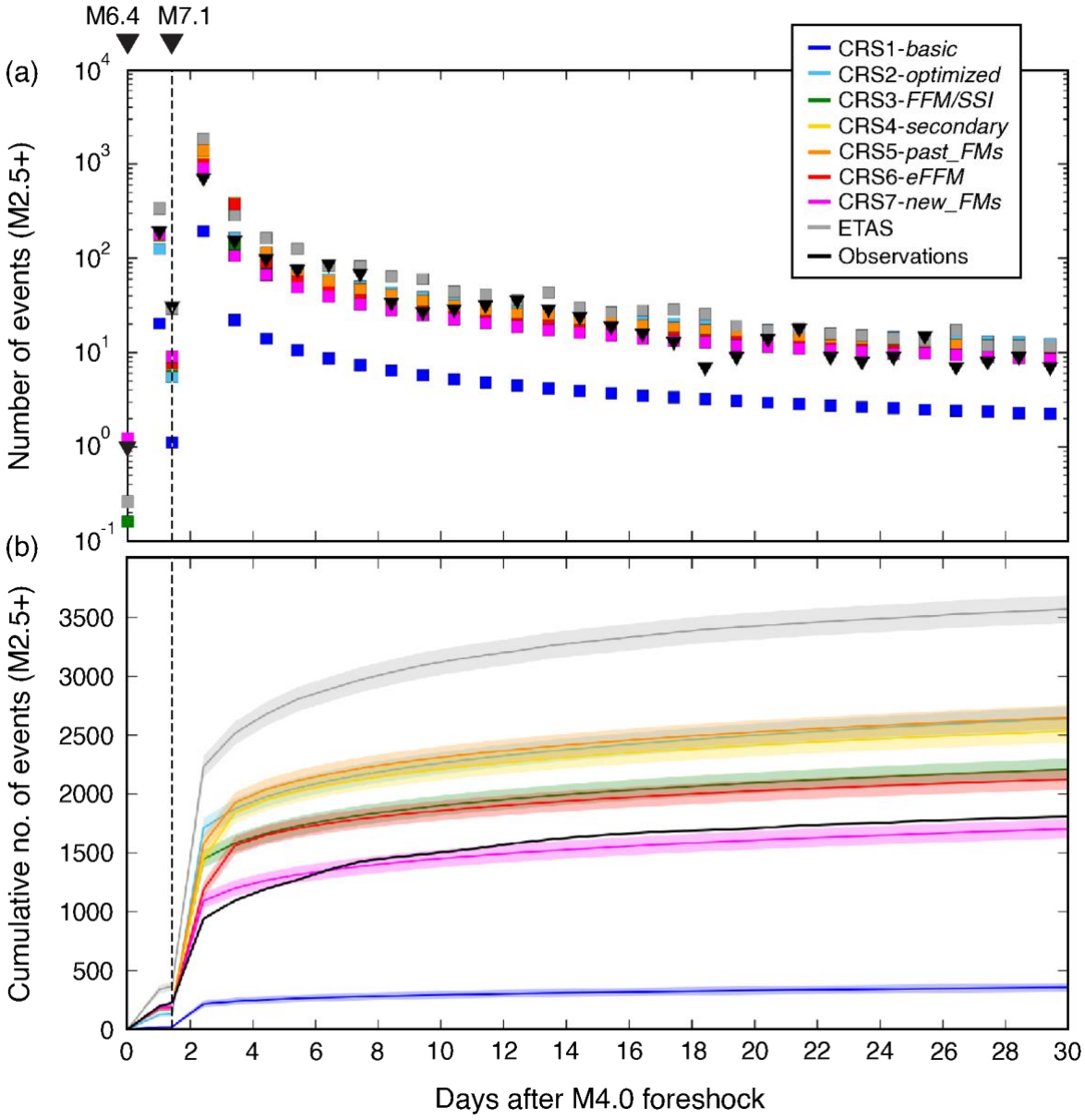

Figure 3. Forecast time series for physics-based and statistical models for the first month of the Ridgecrest sequence. (a) Incremental time series: black triangles indicate the observed number of M2.5+ events, while squares represent the expected numbers. (b) Comparison between the cumulative expected vs. observed (black line) rates. The shaded areas indicate Poissonian uncertainties.

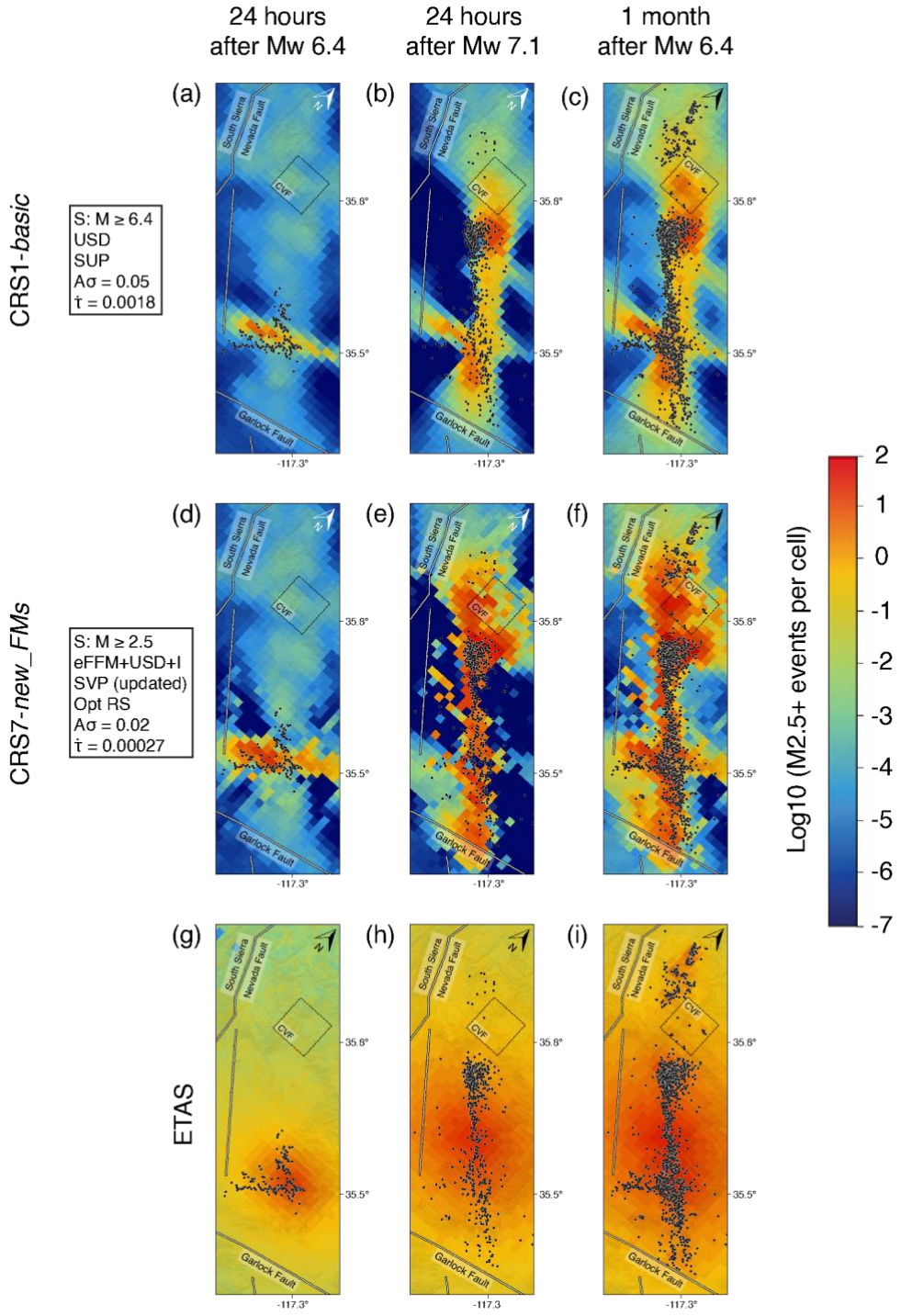

Figure 4. Maps of expected seismicity rates for CRS1/7 and ETAS in the area of main aftershock productivity for the first 24 hours following the two mainshocks and for the first month of the Ridgecrest sequence. Observed events (M2.5+) in each time window are represented as circles.

952 The dashed-line square indicates the area of the Coso volcanic field (CVF). S = sources (minimum
953 magnitude); Opt RS = optimized rate-and-state parameters, USD = uniform slip distribution; SUP
954 = spatially uniform receiver planes; SVP = spatially variable planes; eFFM = edited finite-fault
955 slip model; I = isotropic stress field. Aσ values are in MPa, $\dot{\tau}$ values are in MPa/year.
956
957
958

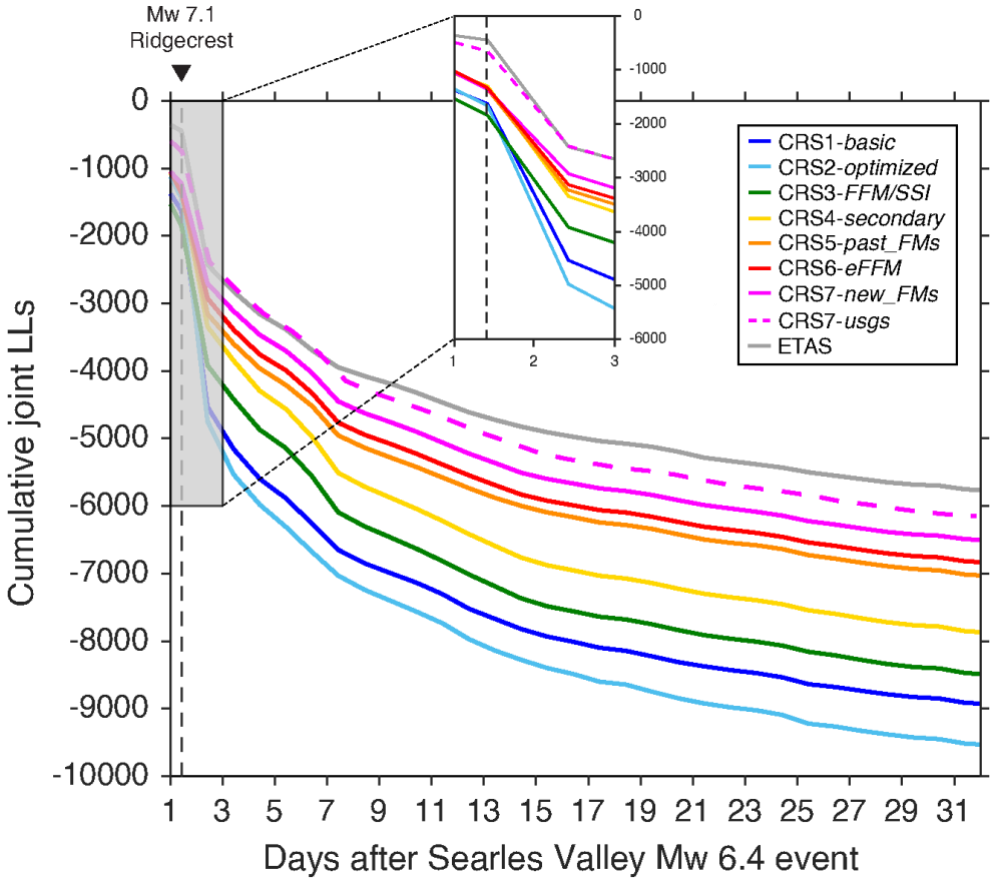

959
960 **Figure 5.** Cumulative S-test joint log-likelihood (jLL_S) timeseries. The scores are obtained by
961 summing the S-test log-likelihoods (LL_S) of each spatial cell and 1-day time step. The vertical
962 dashed line marks the occurrence of the Ridgecrest mainshock.

963

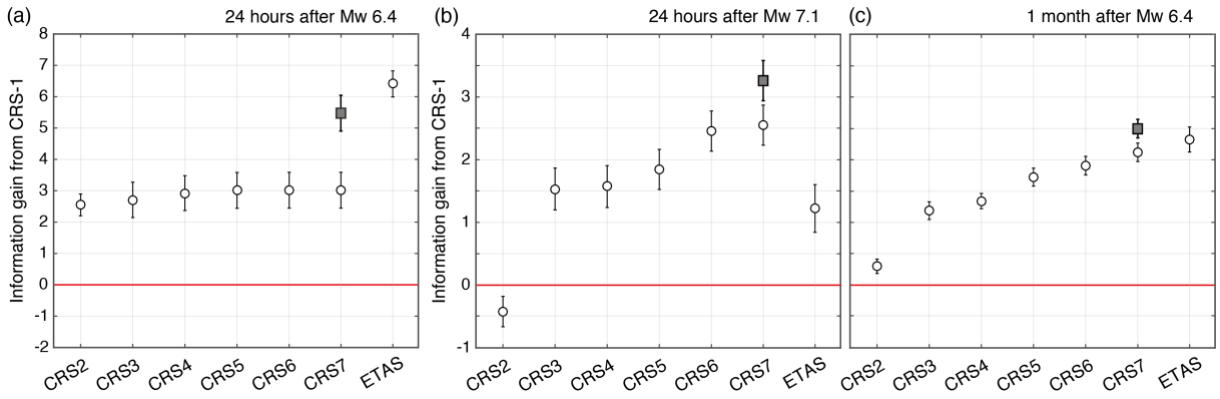

964

965 **Figure 6.** Average daily information gain per earthquake from the preliminary CRS1-*basic* model
966 for: (a) 24 hour after the Mw 6.4 Searles Valley event, (b) 24 hour after the Mw 7.1 Ridgecrest
967 mainshock and (c) for a cumulative 1-month forecast horizon. The filled grey squares indicate the
968 information gain score of the alternative CRS7-*usgs* model. The horizontal lines mark the no-gain
969 level.

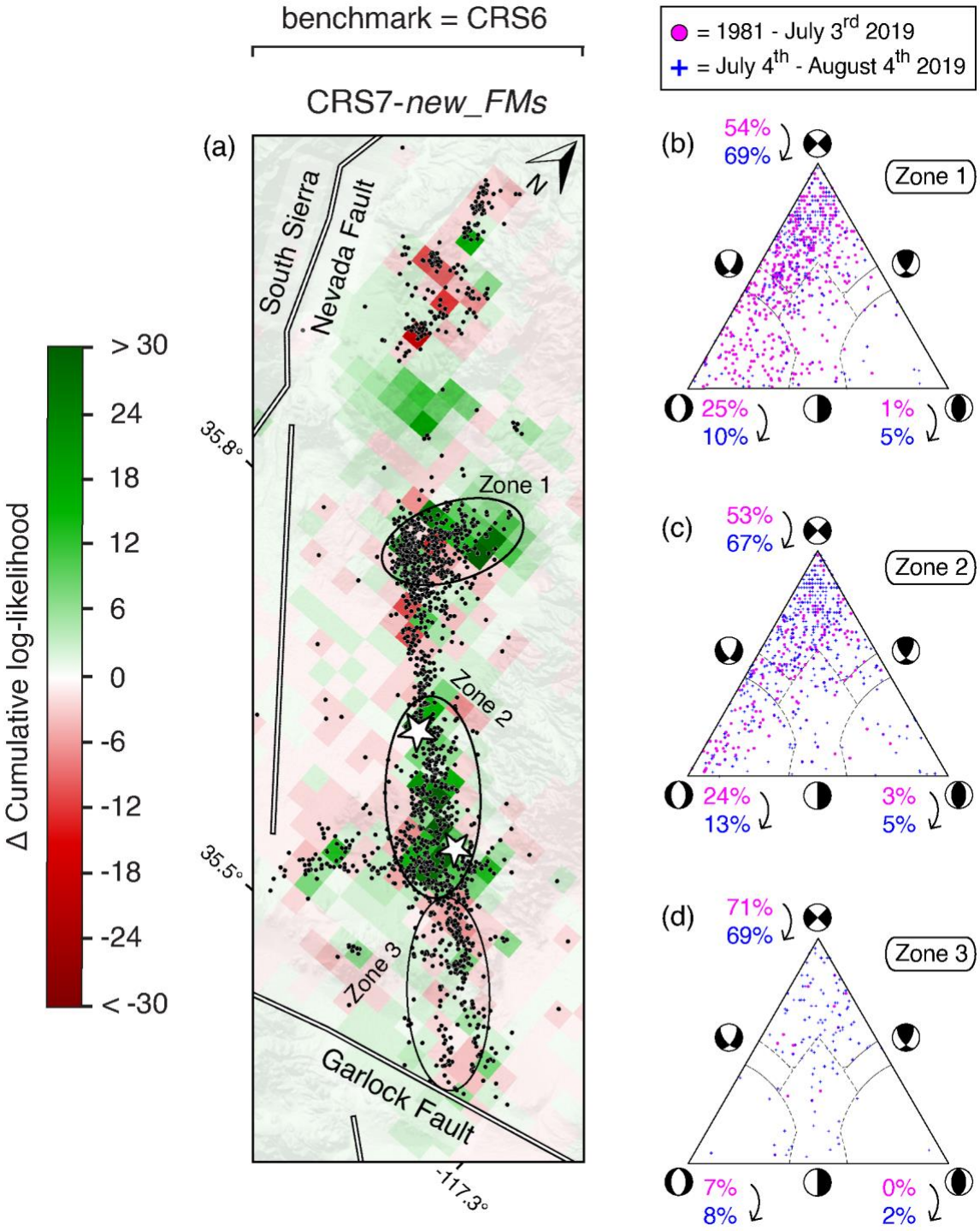

970

971 **Figure 7.** Influence of pre-existing and evolving rupture populations in stress-based forecasts. (a)
972 Map of cumulative ΔLL for the 1-month forecast horizon between CRS6-*eFFM* and CRS7-
973 *new_FMs*. Positive (green) values indicate a better performance of CRS7-*new_FMs*. Black points
974 indicate the locations of M2.5+ aftershocks between 4 July 2019 and 4 August 2019, while white

975 stars represent the two mainshocks. Values are saturated at ±30 to facilitate visualization. (b-d)
976 Ternary diagrams showing the distribution of focal mechanisms during the pre-sequence (1981-
977 2019, magenta circles) and post-Ridgecrest (blue crosses) time windows.